

# Summer 2010 Beam-Halo Overlaps Alignment

Jim Pivarski

October 25, 2010

## 1 Motivation

The “Beam-Halo Overlaps Alignment Method” aligns CSC chambers relative to their neighbors within rings using beam-halo tracks that cross pairs of neighboring chambers. The method has been applied to the following datasets:

- Sep. 2008: “first beam” (9 minutes) with  $\vec{B} = 0$  T, only two rings with zero missing overlaps (ME–2/1, ME–3/1), not uploaded to the database;
- Dec. 2009: “first collisions” (21 days) with  $\vec{B} = 3.8$  T, too few tracks for any alignment due to clean, low-intensity beams;
- Mar. 2010: “Tertiary Collimator Triplet (TCT) test” (40 minutes) with  $\vec{B} = 3.8$  T, new technique uses photogrammetry to fill in missing overlaps, aligned all chambers and uploaded to the database;
- Jun.–Sep 2010: beam-halo during collisions (83 days) with  $\vec{B} = 3.8$  T, repeated with  $\sim 10\times$  the statistics and new  $\phi_y$  alignment derived from collisions to reduce a systematic error. Proposed for upload to the database (with upcoming disk alignment).

This short note describes the last alignment, using data collected by the beam-halo trigger during the most intense LHC beams before the trigger was retired on Sep. 1.

This alignment is only one step in a sequence of endcap alignment steps:

1. photogrammetry pre-alignment (local  $x, y, z, \phi_x, \phi_z$ );
2. SLM lines measurement of disk displacement and bending due to the magnetic field (local  $z, \phi_x$ , replacing photogrammetry);
3. “missing angle measurement” from collisions (local  $\phi_y$ );
4. beam-halo alignment of chambers relative to rings, combined with PG to fill in data in missing chambers ( $r\phi \approx x$  and  $\phi_z$ , replacing photogrammetry);
5. disk alignment using collisions (global  $x, y, \phi_z$  of whole disks, keeping internal chamber structure intact, for YE1 and YE2);
6. disk alignment using straight-through collisions (global  $x, y, \phi_z$  of whole disks for YE3 relative to YE2).

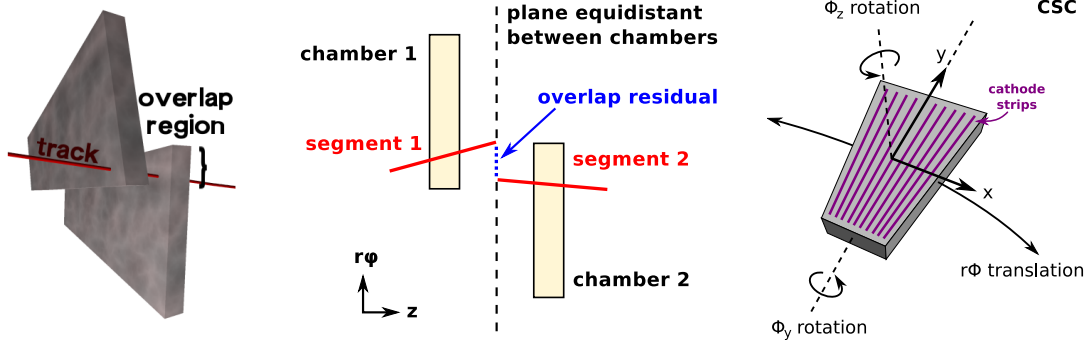


Figure 1: Left: illustration of a track passing through the overlap region. Middle: diagram indicating how the overlap residual is defined. Right: coordinates of a chamber position that are relevant for this alignment.

## 2 Reminder of the method

CSC chambers in each station overlap each other slightly along their edges, in part to provide short tracks for alignment. Tracks passing through the overlap region do not encounter any thick material, so their trajectories can be accurately propagated between the chambers. Track-segments constructed from hits in each chamber individually are linearly extrapolated to a plane equidistant between them, and the  $r\phi$  difference between their points of intersection is called the overlap residual. A bias in the distribution of overlap residuals indicates a relative misalignment of the two chambers. Figure 1 summarizes these definitions.

To compute relative corrections to the positions of all chambers in a ring from these pairwise constraints, we minimize the following:

$$\chi^2 = \sum_{m_{ij}}^{\text{constraints}} \frac{(m_{ij} - A_i + A_j)^2}{\sigma_{ij}^2} + \lambda \left( \frac{1}{N_{\text{chambers}}} \sum_i^{\text{chambers}} A_i \right)^2 \quad (1)$$

where  $m_{ij}$  is a constraint between chambers  $i$  and  $j$  and  $\sigma_{ij}$  is its uncertainty (the constraint is statistically satisfied if  $|m_{ij}/\sigma_{ij}| \sim 1$ ),  $A_i$  and  $A_j$  are chamber position corrections, and the last term is a Lagrange multiplier to make the system solvable by enforcing an arbitrary coordinate system ( $\lambda$  is an arbitrary constant: the only alignment results that are physically meaningful do not depend on  $\lambda$ ). Beam-halo tracks (BH) provide one of the two sets of constraints: the mean of each overlaps residuals distribution is required to be zero. Since tracks in CSC overlap regions only relate chambers relative to their immediate neighbors, each of these constraints relates chambers  $i$  and  $j = i + 1$  (or  $j = 1$  if  $i = N_{\text{chambers}}$ ).

The above formalism would be sufficient to align all chambers in a ring if no overlaps were missing. However, several of the 400 chamber-overlaps in the muon endcap are not read out due to electronics issues (see next section). Photogrammetry (PG) measurements from 2007 supplement the beam-halo data in order to fill in the gaps. PG constraints relate each chamber  $i$  with an external reference, treated as a new alignable  $A_{\text{PGFrame}}$ . PG data are applied in two ways: (1) all available PG data are included in the fit, weighted appropriately with BH according to their uncertainties, and (2) only PG measurements necessary to fill gaps in BH are applied.

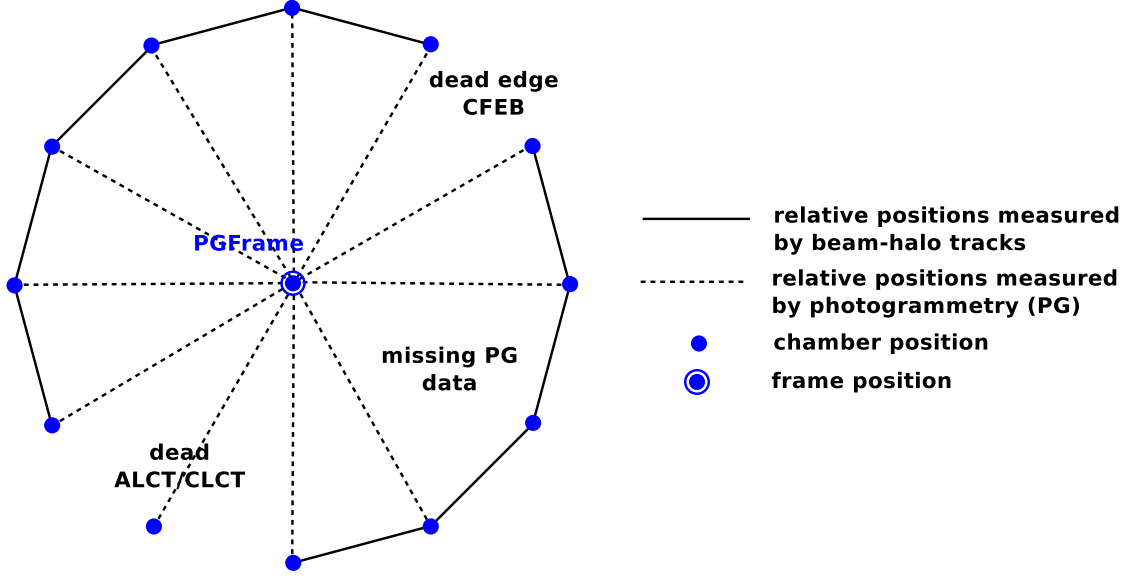


Figure 2: Schematic diagram showing how beam-halo (BH) and photogrammetry (PG) data are combined. Each point represents an alignable  $A_i$  (most of which are chambers, one is an abstract point “PGFrame”) and each edge represents a measurement constraint  $m_{ij}$  between alignables  $A_i$  and  $A_j$ . Alignment of all alignables in a single coordinate system is possible if the graph is fully connected. Otherwise, coordinate systems for each connected subgraph “float freely” with respect to one another.

Figure 2 illustrates this procedure as a graph: only fully connected graphs are solvable. Sometimes we wish to study the alignment of a disconnected graph (e.g. ME1/1 and alignments without PG constraints); in those cases, we add a Lagrange multiplier (with separate  $\lambda_i$ ) for each missing overlap. Disconnected groups are said to “float freely” with respect to one another ( $\lambda_i$  may be tuned arbitrarily: it does not represent a real alignment result).

The objective function in Eqn. 1 is minimized by setting its derivatives to zero, which forms an  $N_{\text{alignables}} \times N_{\text{alignables}}$  matrix where  $N_{\text{alignables}} = 18$  or 36, and numerically solving the resulting matrix equation. The chamber corrections  $A_i$  in the solution are highly correlated, but the correlated statistical uncertainties can be decomposed into a set of statistically independent modes. That is, the vector  $\vec{A}$  can be written in a new basis as  $\vec{B}$ , in which each  $B_i$  is a linear combination of all  $A_i$  and graphically looks like a coherent, global distortion of the entire ring. The change of basis was designed such that each  $B_i$  has a statistically independent uncertainty. The  $B_i$  with the largest uncertainties are called the weakest modes.

### 3 Details of the dataset and method

#### 3.1 Summer 2010 dataset

Unlike previous beam-halo alignments, the summer 2010 data were collected over a long time period, while the beams were colliding. A special trigger was designed to collect beam-halo

data during collisions, though the beam-halo AlCaReco stream accepted muons from all muon triggers (“HLT\_CSCBeamHaloOverlapRing1 OR HLT\_CSCBeamHaloOverlapRing2 OR HLT\_L1Mu\* OR HLT\_L2Mu\* OR HLT\_Mu\* OR HLT\_L1MuOpen\*”), so it is possible that some of the muons used in this analysis were from  $pp$  collisions, rather than beam-halo. It is not necessary for the sample to be purely beam-halo—only the topology is important: nearly horizontal tracks with relatively high momentum.

Figure 3 presents the occupancy distribution of CSC overlaps with the March 2010 TCT test (pure beam-halo in a 40-minute run) as a reference. Note that each “overlap” corresponds to a pair of chambers, not a single chamber (so a whole missing chamber results in two missing overlaps). Every missing overlap (zero or only several hits) was diagnosed in March; each had a cause that could be traced to an electronics issue. In the summer data, seven of the ME1/1 overlaps were fixed (5 with low HV in a single layer, 2 with low CFEB efficiency on the edge of a chamber), and one new problem was introduced in ME–1/2. This change in the pattern of missing chambers in ME1/1 significantly affected the results (where gaps are not controlled by PG).

### 3.2 Selection criteria

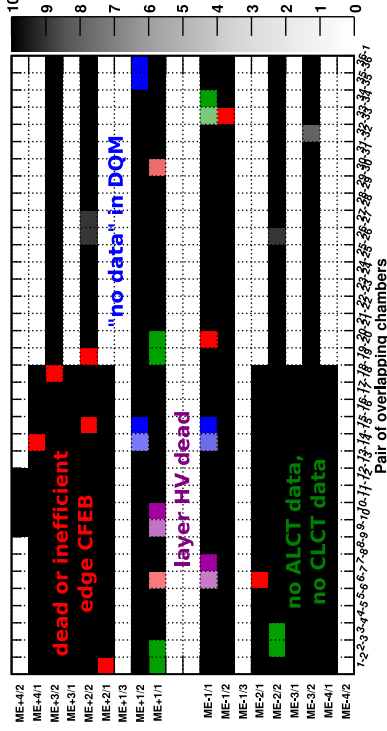
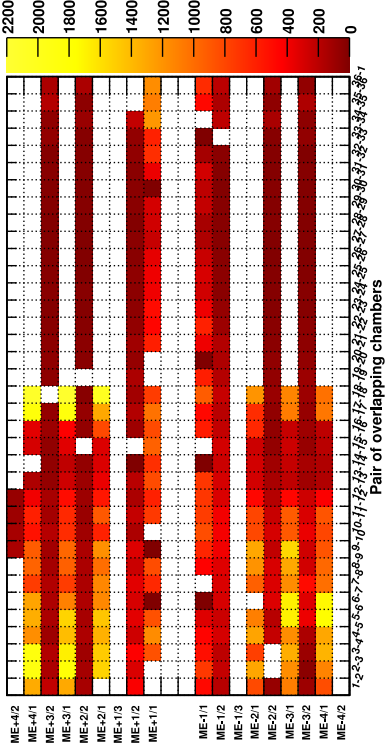
To select well-behaved muons (muons whose trajectory can be accurately propagated from one chamber to its neighbor), we require the muons to have momenta of several tens of GeV/ $c$  or higher. Horizontal muons are parallel with the axial magnetic field of CMS, so all momentum information comes from the radial component of the magnetic field. To determine how well true momentum can be estimated from the offline track-fit, an MC sample of horizontal muons was simulated. Figure 4-a shows the distribution of reconstructed momenta as a function of true momentum, and Fig. 4-b shows the efficiency of a reco-level cuts as a function of true momentum. With a 20 GeV/ $c$  reco-level cut, the efficiency for 10 GeV/ $c$  muons is less than 20%, dropping to zero efficiency for very low-momentum muons. Figure 4-c shows the reco-level momenta in data with the  $|\vec{p}| < 20$  GeV/ $c$  cut used in the analysis.

To select horizontal muons, we applied a cut on the entrance angle of track-segments in the  $r$ - $z$  plane. This angle may be described as  $dr/dz$  where  $r$  is the radius of hits in the segment and  $z$  is the component parallel with the beamline. Muons from the interaction point have  $|dr/dz| > 0.12$  rad, which corresponds to  $|\eta| < 2.4$  ( $|dr/dz| \rightarrow \infty$  implies  $\eta \rightarrow 0$ ). Figure 5 presents the  $dr/dz$  distribution observed in three datasets: Dec. 2009 (which had an open trigger and was dominated by cosmic rays), Mar. 2010 (which had an open trigger and was dominated by beam-halo), and summer 2010 (which had a tight trigger and contains both beam-halo and collisions). A  $|dr/dz| < 0.2$  rad cut was used in the Mar. 2010 analysis, but this cut was tightened to  $|dr/dz| < 0.12$  for the analysis described in this note, to exclude muons that point to the beamspot.

Tracks and hits used in this analysis also required the following:

- at least 5 hits per chamber (which has 6 layers);
- fitted track-segment must stay within the fiducial region of each chamber:  $|\phi| < 0.086$  for ME1/1,  $|\phi| < 0.090$  for ME1/2,  $|\phi| < 0.180$  for ME $x$ /1, and  $|\phi| < 0.090$  for ME $x$ /2,

March 2010 (40-minute LHC TCT test)



Jun-Sep 2010 (beam-halo during collisions)

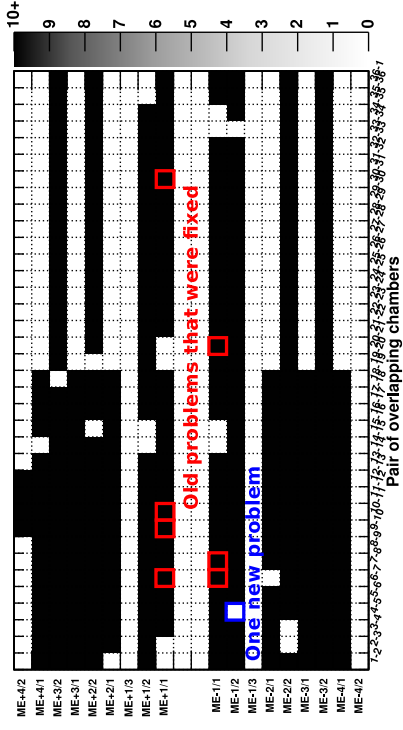
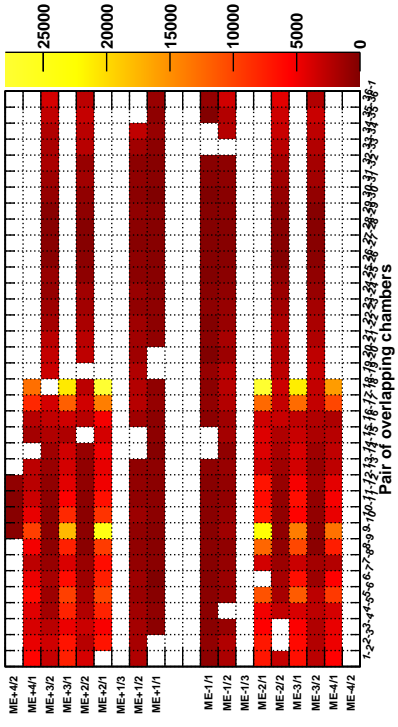


Figure 3: Occupancy maps of CSC chambers during the March special beam-halo run (left) and the most intense period of beam with the beam-halo-during-collisions trigger (right). The top plots show number of hits in the color scale and the bottom plots show the same with a color scale saturated by 10 or more hits, to identify inactive CSCs. Each inactive CSC was diagnosed in March (reasons for no read-out are given on the plot). In the summer data, 7 previously inactive ME1/1 chambers are now reading out data, and 1 previously active ME-1/2 chamber is now inactive.

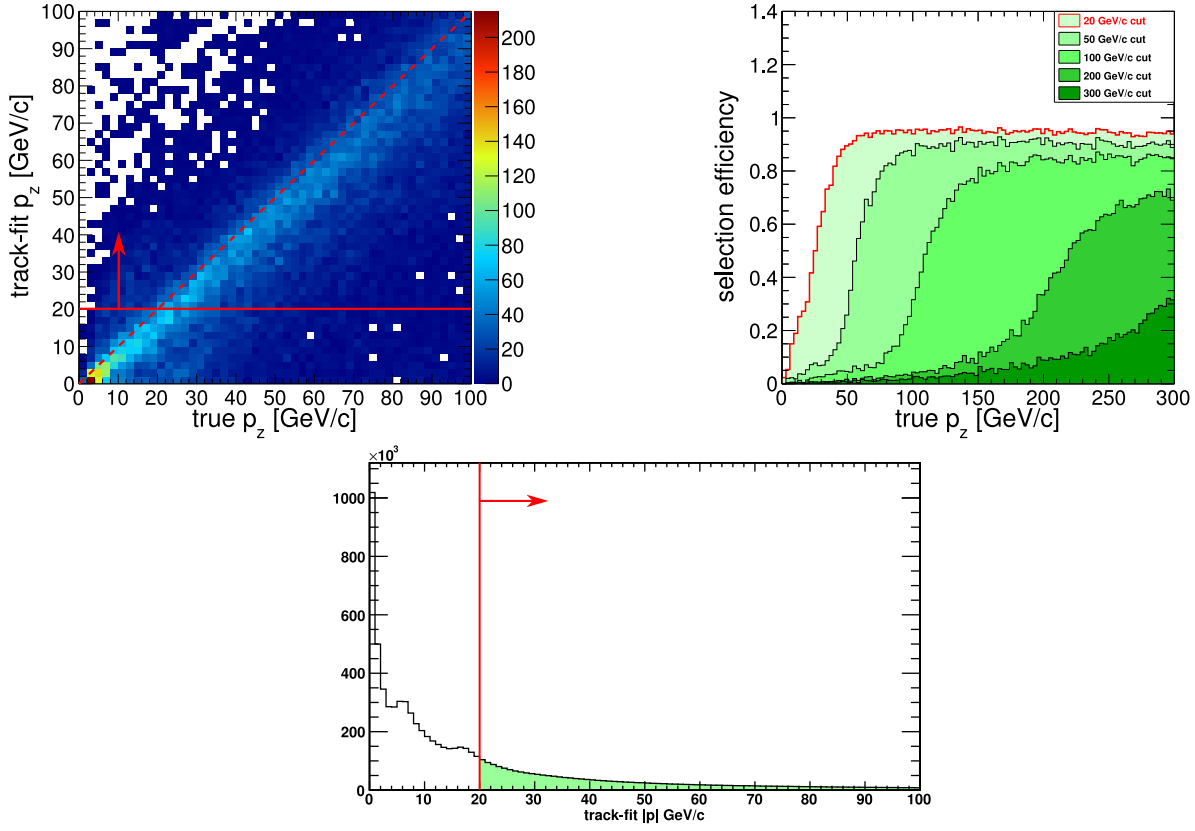


Figure 4: Top-left: reconstructed track momentum ( $p_z$ ) versus true track momentum in MC. Top-right: efficiency as a function of true track momentum with a  $p_z > 20$  GeV/c cut in MC. Bottom: distribution of reconstructed track momentum ( $|\vec{p}|$ ) in data.

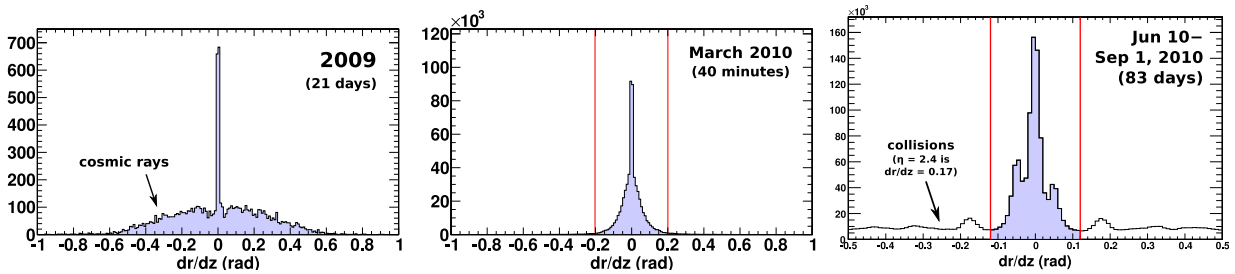


Figure 5: Track entrance angles  $dr/dz$  where  $r$  is the radial component and  $z$  is parallel with the beamline, for 2009 data (left), March 2010 data (middle), and summer 2010 data (right, with a narrower window). Each has different background components and different trigger conditions.

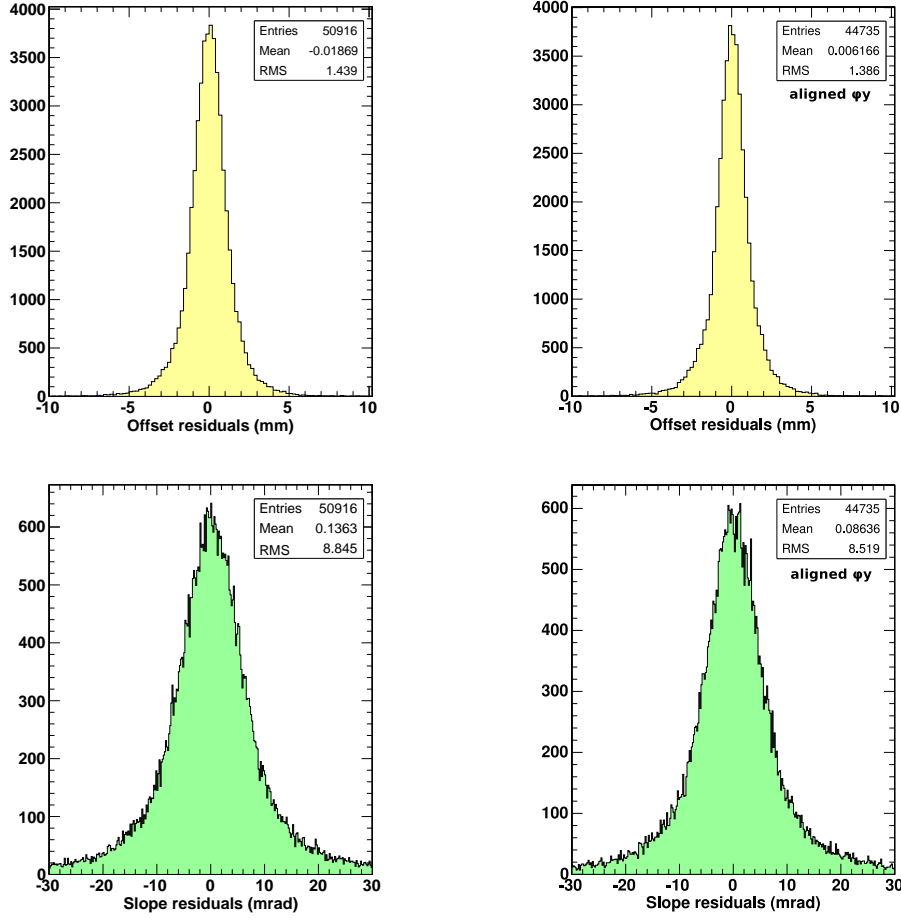


Figure 6: Offset residuals without (top-left) and with (top-right)  $\phi_y$  pre-alignment, and slope residuals without (bottom-left) and with (bottom-right)  $\phi_y$  pre-alignment.

where  $\phi$  is the difference in azimuthal position between the track-segment position and the center of its chamber and  $x \geq 2$ ;

- “offset residuals,” the difference in propagated  $r\phi$  position at the common plane between the two chambers, must have a magnitude less than 15 mm;
- “slope residuals,” the difference in  $d(r\phi)/dz$  angle for the two track-segments in an overlap, must be less than 30 mrad.

Figure 6 presents the offset residuals and slope residuals, with and without  $\phi_y$  pre-alignment. Since most of the  $\phi_y$  corrections were only a few mrad and the overlaps measurement has a resolution of 8 mrad, the improvement is not visible.

### 3.3 Other details of the method

Hit weights were used to fit track-segments, but no weighting was used to determine the average offset residual in each overlap— only a truncated mean. Only overlaps with ten or more muons were used to constrain the alignment, and uncertainties in offset-residuals means were calculated as  $\text{RMS}/\sqrt{N_{\text{overlap muons}}}$ .

Coordinates were individually aligned in several passes. The first pass adjusted the radius of each ring such that the sum of all overlap-residuals means is zero. The next four passes alternately align  $r\phi$  and  $\phi_z$ ; for example, in the second pass,  $A_i$  and  $A_j$  in Eqn. 1 represent  $r\phi$  corrections, while in the third pass, they represent  $\phi_z$  corrections. The fourth and fifth passes over  $r\phi$  and  $\phi_z$  are just to verify that the two parameters have converged: no large changes are observed after the third pass.

## 4 Results and comparison to old data

The following alignments were performed:

- BH+PG alignment using data from Mar. 2010 TCT test (currently the official geometry in the database);
- BH+PG under the same conditions as above, but using summer 2010 data;
- summer 2010 alignment like the above but the new hardware  $z/\phi_x$  values;
- summer 2010 alignment like the above but also using the new  $\phi_y$  pre-alignment from collisions;
- BH-only summer 2010 alignment with no input from PG (yet otherwise like the above);
- BH+PG-only-in-gaps alignment: PG data were only used where BH overlaps do not exist.

Each subsection compares the results from one of these geometries with the previous. Histograms of differences in  $r\phi$  and  $\phi_z$  are presented first, followed by differences versus chamber number for the rings with the largest deviations, to look for a pattern. In cases in which differences are negligible (much less than 1 mm or 1 mrad), only the histogram is shown.

Chambers are classified in three groups: ME1/1, inner (ME1/2 and ME $x$ /1), and outer (ME $x$ /2), where  $x \geq 2$ . Chambers within each of these groups are affected by different considerations: ME1/1 have no PG constraint, inner chambers have the highest beam-halo statistics, and outer chambers have lower beam-halo statistics. Three histograms will therefore be filled in each study, one for each class of chambers.

### 4.1 Comparison of March (TCT) results with summer results

The Mar. 2010 TCT run was a special run of the LHC designed to produce high rates of beam-halo. Both LHC beams were completely converted into beam-halo muons in 40 minutes. This provided a pure sample of beam-halo used early in the year to produce an initial



CSC geometry, and it is still the official chambers-within-ring geometry used for CMSSW reconstruction. The summer 2010 data were collected over a longer time period during collisions data-taking. We do not expect significant motion of the chambers between March and the summer, and observed differences cannot be easily interpreted as physical motions because of the changes in conditions (trigger, available BH overlaps, and slightly tighter  $|dr/dz|$  window: see Figs. 3 and 5).

Figure 7 presents differences between the March alignment and the summer alignment. The largest differences are in ME1/1 and can be attributed to new overlap measurements that were not available in March (especially in ME+1/1). A group of chambers in ME+1/1 between 7 and 30 (inclusive) rotated around the beamline by 1 mm with respect to the others: this region is bordered by two overlaps measurements that were not available in March but now are (see Fig. 3). Outer chambers have larger differences between the two datasets than inner chambers, but without a clear pattern.

Figure 8 shows the same for  $\phi_z$ , which has structures bordered by missing BH data, just as in  $r\phi$ . Differences in all other rings are completely negligible.

## 4.2 Comparison of results based on old and new hardware pre-alignment

In the second study, we aligned the same data (summer 2010) using two pre-alignments: one with the old hardware  $z/\phi_x$  description and the other with the new description. As can be seen in Fig. 9, there are no differences in ME1/1 (since there were no  $z/\phi_x$  differences in ME1/1) and only minor effects in the other rings, ranging from 0.3–0.5 mm (RMS). Figure 10 shows the same for  $\phi_z$ , where all differences are completely negligible.

## 4.3 Comparison of results with and without $\phi_y$ pre-alignment

The next test compared two geometries aligned with the same data (summer 2010) using two pre-alignments: one with  $\phi_y$  corrections derived from data, and the other without. One might imagine  $\phi_y$  differences to have an effect on  $r\phi$ , since this angle would bias the slope of all segments in a chamber (see Fig. 1). However, the slope resolution is 8 mrad and  $\phi_y$  corrections were typically only a few mrad (see Fig. 6), so the result is not particularly sensitive to these changes. Figures 11 and 12 show the  $r\phi$  and  $\phi_z$  sensitivity to the  $\phi_y$  pre-alignment: about 0.25–0.5 mm in  $r\phi$  and negligible in  $\phi_z$ .

## 4.4 Comparison of results with and without PG constraint

The effect of the PG constraint was tested by aligning the same data (summer 2010) with and without the constraint. Without the constraint, groups of chambers connected by BH overlap data are mutually aligned, but disconnected groups are allowed to float relative to one another. Figure 13 shows no difference in ME1/1 due to the fact that no PG constraint was applied in either case, small differences in the inner chambers, which are dominated by beam-halo measurements, and large differences in the outer chambers. By plotting each of the outer rings versus chamber number (in the same figure), we see that these differences have clear global patterns. In ME+2/2, there are two independent groups, one of which

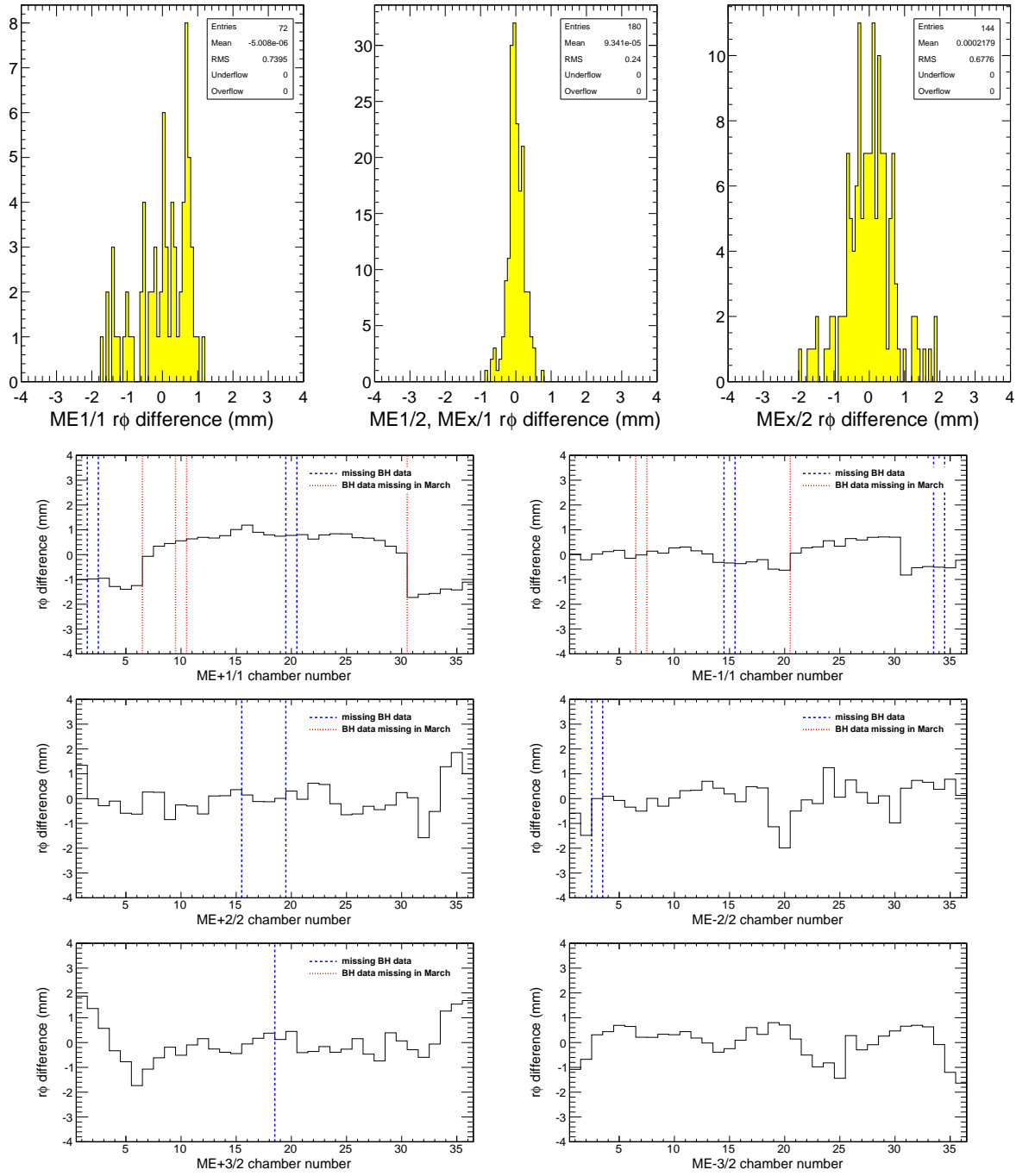


Figure 7: Differences in  $r\phi$  parameters between the Mar. 2010 TCT alignment and the summer 2010 during-collisions alignment. The largest differences are in ME+1/1, where two new overlaps measurements became available (6-7 and 30-31) and shifted everything in between them coherently. No systematic changes in shape were observed in ME2/2 and 3/2, though the size of the changes are 0.6 mm (RMS).

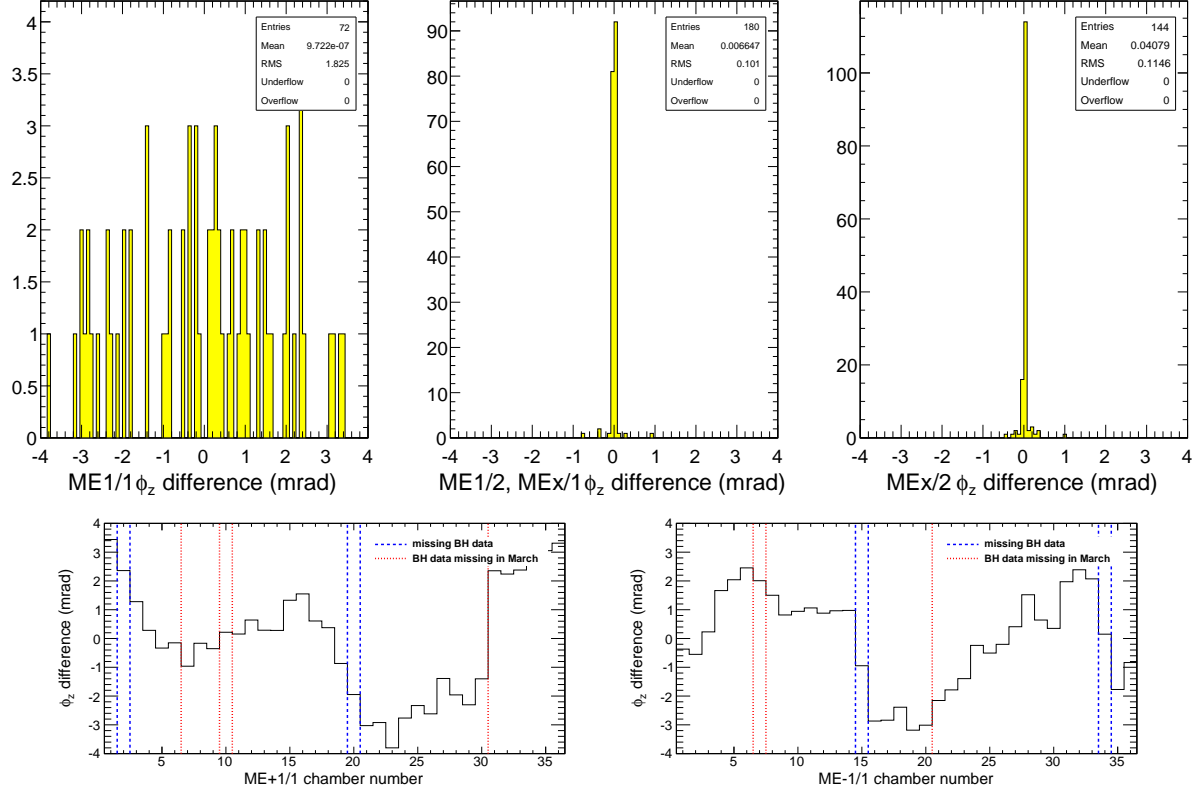


Figure 8: Differences in  $\phi_z$  parameters between the Mar. 2010 TCT alignment and the summer 2010 during-collisions alignment. The largest differences are in ME $\pm$ 1/1, usually near the missing overlaps measurements. Changes in all other rings are completely negligible.

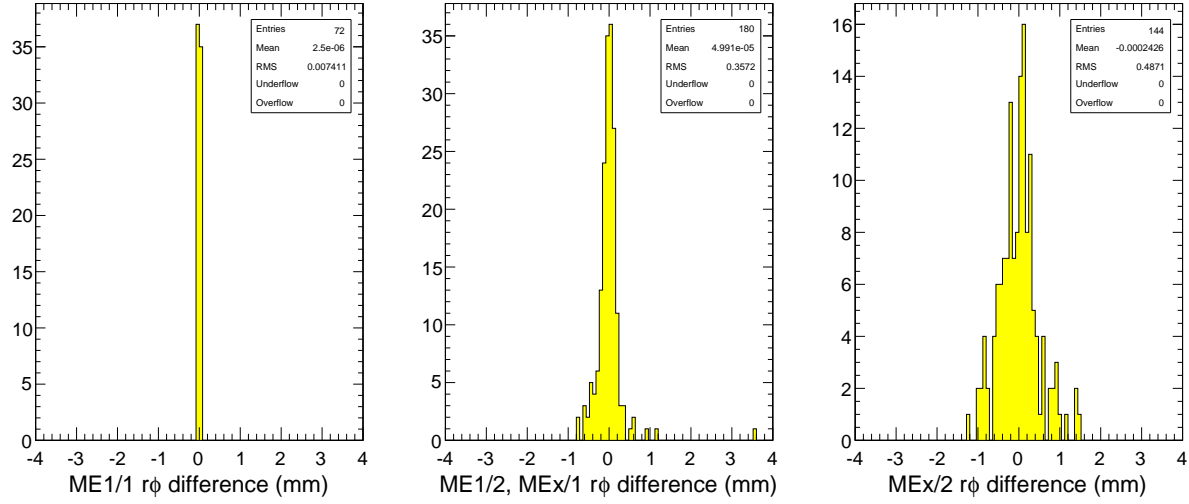


Figure 9: Differences in  $r\phi$  parameters between a summer 2010 alignment with old HW  $z/\phi_x$  description and the new HW  $z/\phi_x$  update. No changes in these parameters were made in ME1/1, so ME1/1 are exactly the same. Other rings are sensitive at the level of 0.3–0.5 mm (RMS).

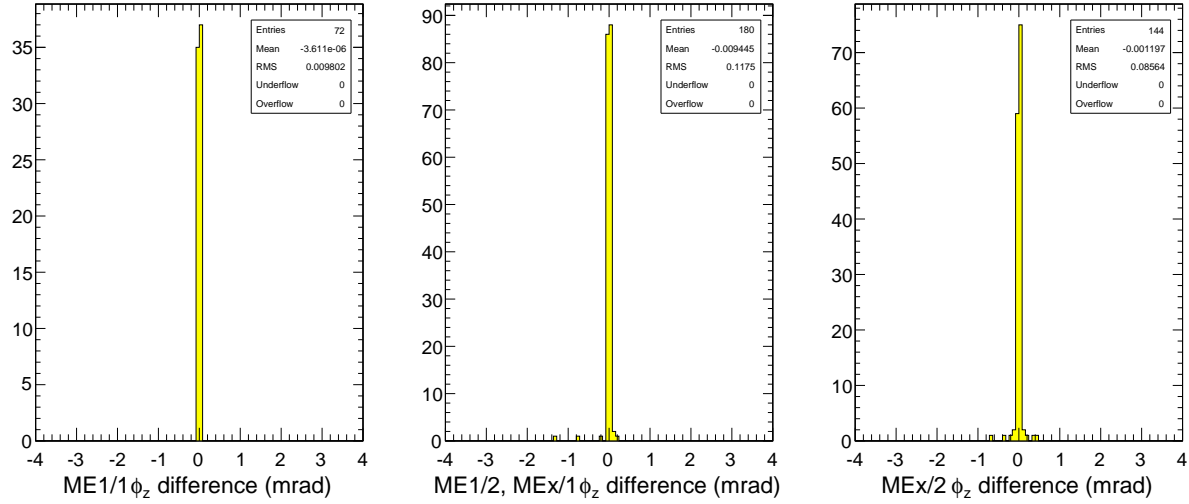


Figure 10: Differences in  $\phi_z$  parameters between a summer 2010 alignment with old HW  $z/\phi_x$  description and the new HW  $z/\phi_x$  update. All  $\phi_z$  differences are completely negligible.

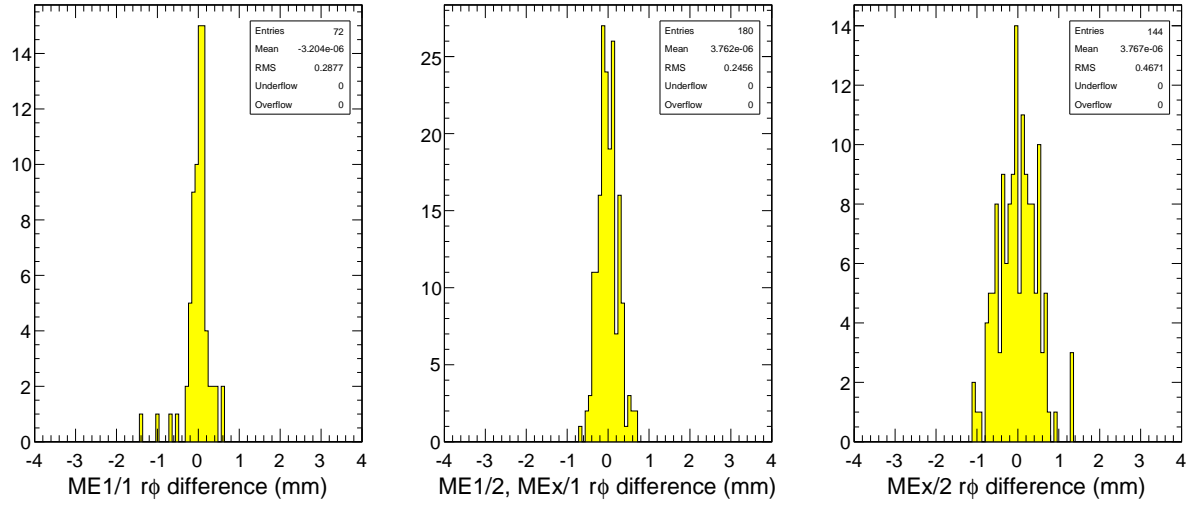


Figure 11: Differences in  $r\phi$  parameters between a summer 2010 alignment with and without  $\phi_y$  pre-alignment. The  $r\phi$  differences are sensitive at the level of 0.25–0.5 mm (RMS).

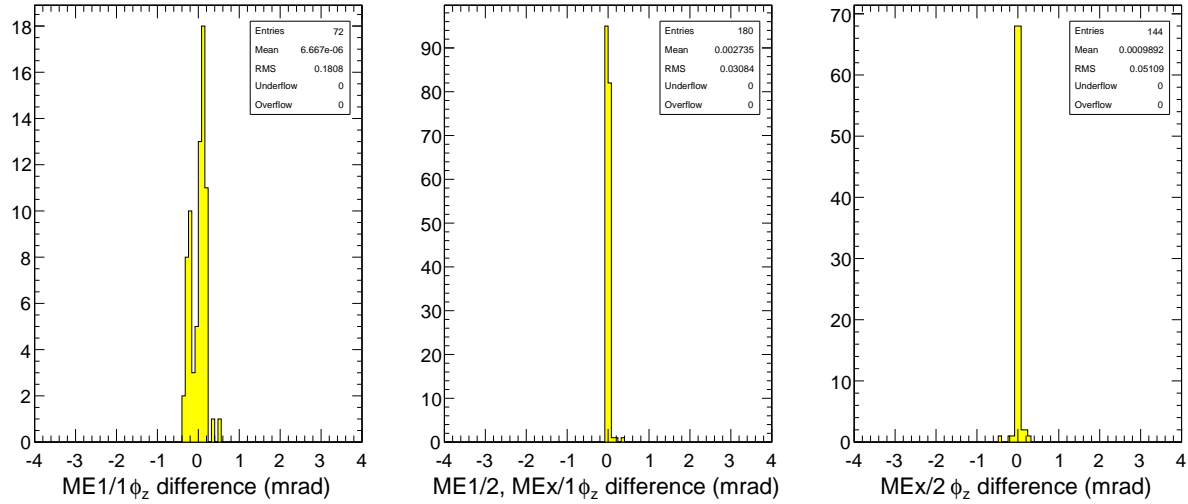


Figure 12: Differences in  $\phi_z$  parameters between a summer 2010 alignment with and without  $\phi_y$  pre-alignment. All  $\phi_z$  differences are completely negligible.

Table 1: Summary of uncertainties in alignment without PG constraint.

Ring	Number of modes	Largest mode uncertainty	Sum in quadrature
ME+1/1	32 modes	1.13 mm	1.69 mm
ME+1/2	32 modes	0.44 mm	0.62 mm
ME+2/1	17 modes	0.15 mm	0.19 mm
ME+2/2	34 modes	1.40 mm	1.74 mm
ME+3/1	17 modes	0.08 mm	0.14 mm
ME+3/2	35 modes	1.62 mm	2.00 mm
ME+4/1	17 modes	0.16 mm	0.21 mm
ME+4/2	3 modes	0.30 mm	0.34 mm
ME−1/1	32 modes	0.86 mm	1.28 mm
ME−1/2	34 modes	0.55 mm	0.73 mm
ME−2/1	17 modes	0.16 mm	0.20 mm
ME−2/2	34 modes	1.44 mm	1.73 mm
ME−3/1	17 modes	0.09 mm	0.14 mm
ME−3/2	35 modes	0.83 mm	1.15 mm
ME−4/1	17 modes	0.09 mm	0.15 mm

ranges between chambers 16 and 19 (inclusive) and floats 1–2 mm relative to the other group. ME+3/2 has a global deformation with an amplitude of 3 mm, and ME−3/2 has a global deformation with an amplitude of 1 mm. Similar plots for  $\phi_z$  are shown in Fig. 14.

The outer-ring differences between PG-constrained and non-PG-constrained alignments look like weak modes, so we plot the shapes of the eight weakest modes in each ring in Fig. 15 (non-PG-constrained alignment). Since ME+2/2 and ME−2/2 each have two disconnected regions, they each have two trivial modes deriving from the Lagrange multipliers: one represents the fact that rotations of the whole ring are unconstrained and the other represents the fact that the two disconnected regions are unconstrained relative to one another. ME+3/2 and ME−3/2 each have one trivial mode due to unconstrained rotations of the ring only. In these plots, each of the normalized modes has been multiplied by the uncertainty in the mode to give a sense of how they compare to one another. A table of the largest mode in each ring and the sum in quadrature of all modes in each ring are given in Table 1. We see from this table that outer ring statistical uncertainties are about ten times larger than inner ring statistical uncertainties.

There are two possible explanations for the global distortions in ME±3/2:

- they are weak modes of the alignment procedure using BH data only, and are minimized by adding PG constraints;
- they are a true deformation of the disk that occurred sometime between 2007 (when the PG data were collected) and 2010 (when the BH data were collected).

The best way to resolve this question is to look at both geometries in an independent dataset. The 3 mm amplitude of ME+3/2 (and possibly the 1 mm amplitude of ME−3/2) is large enough to be seen from collisions. This study is forthcoming.

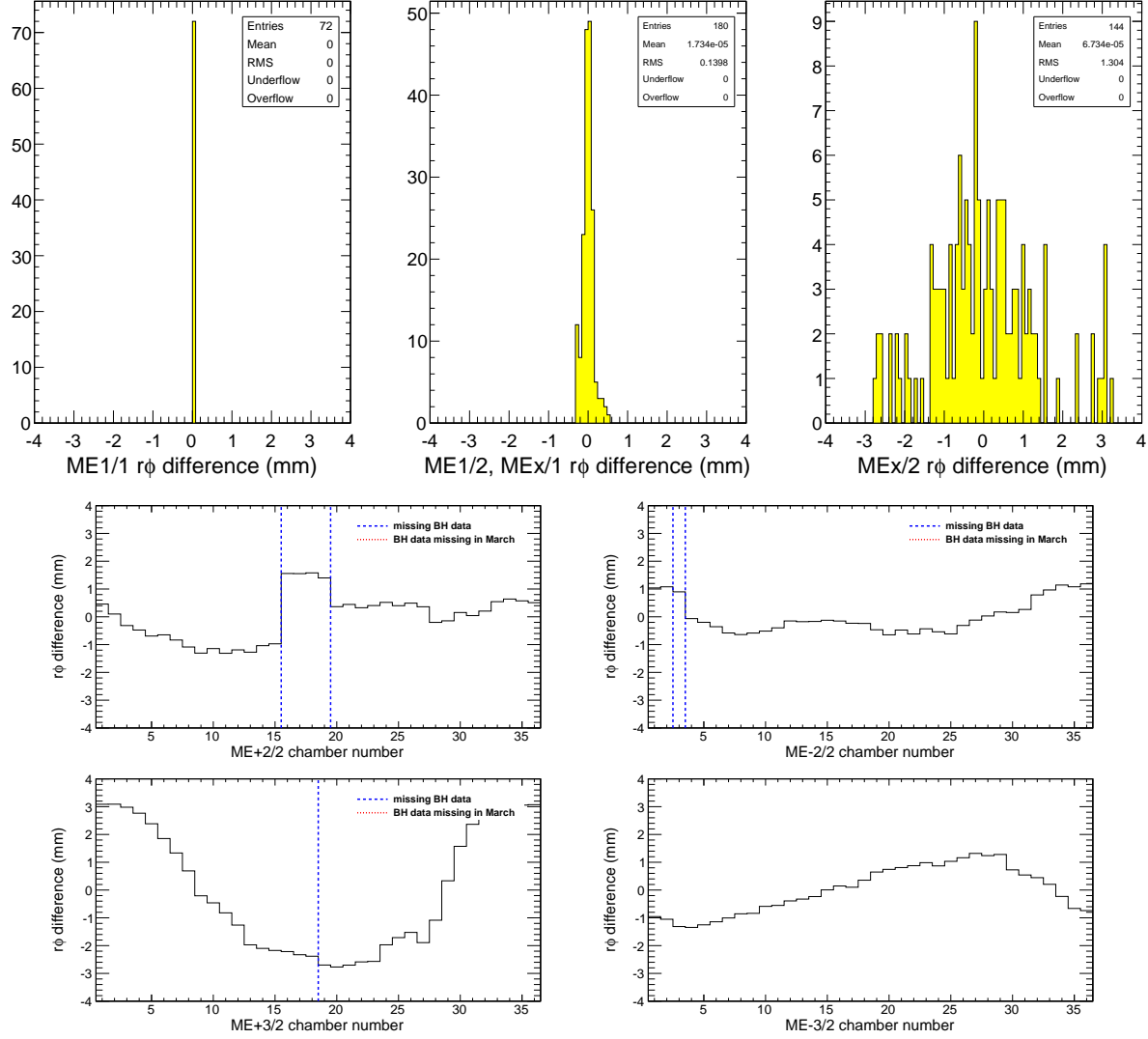


Figure 13: Differences in  $r\phi$  parameters between a summer 2010 alignment with and without PG constraint. ME1/1 chambers have no PG constraint, so they are unaffected, and differences in inner-ring chambers are also negligible. However, the outer rings differ systematically: ME+2/2 has two missing BH overlaps that benefit from the PG constraint, and ME $\pm$ 3/2 have global distortions that are suppressed by the PG constraint.

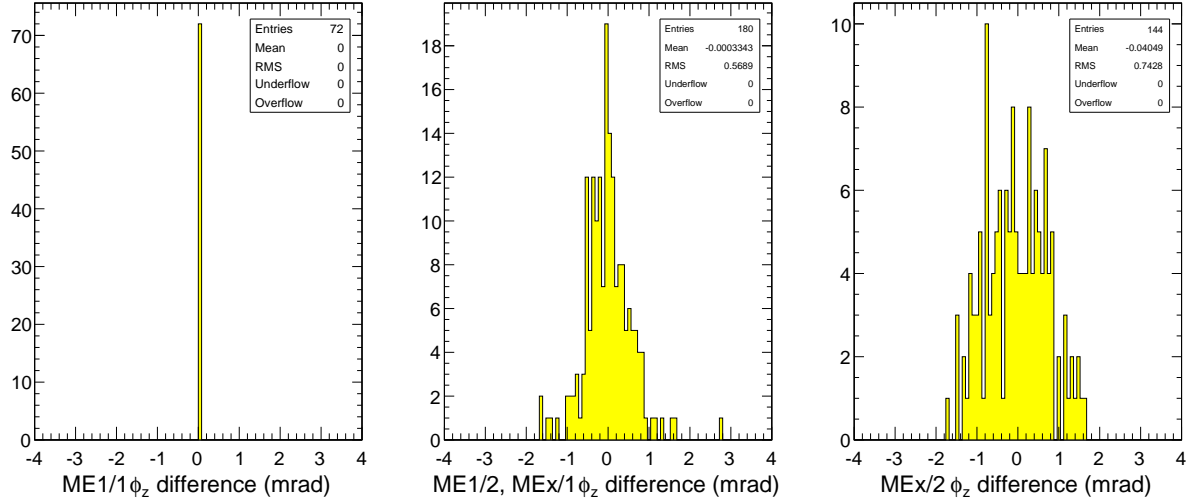


Figure 14: Differences in  $\phi_z$  parameters between a summer 2010 alignment with and without PG constraint. ME1/1 chambers have no PG constraint, so they are unaffected. Differences in other rings are at the level of 0.5–0.8 mrad (RMS).

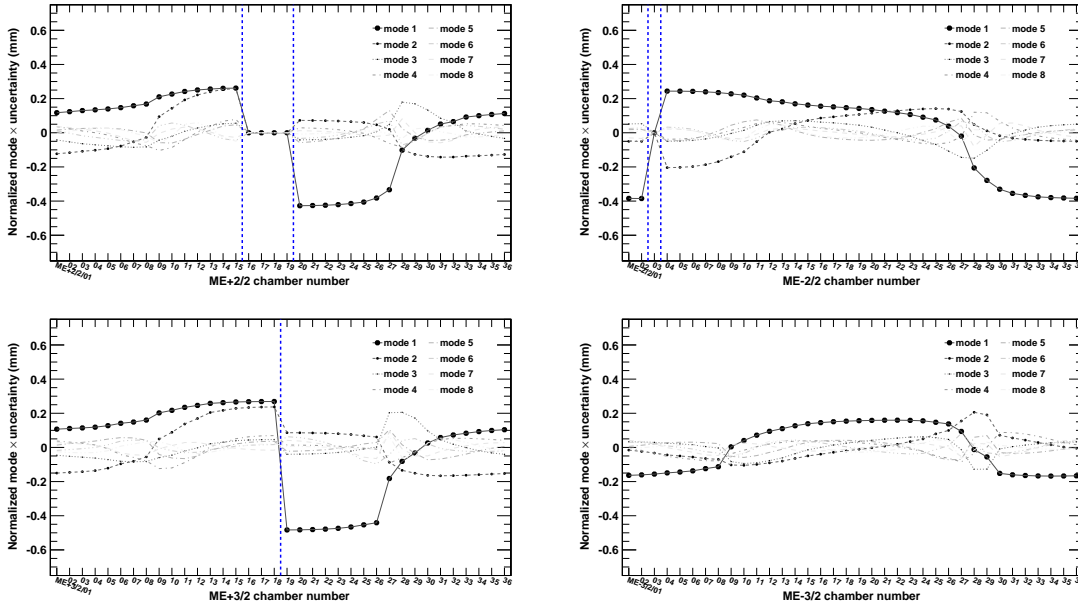


Figure 15: Statistical uncertainties in outer chambers without any PG constraint, expressed as uncorrelated normal modes. Only the eight weakest (non-trivial) modes are shown. Vertical dashed lines indicate neighboring chambers without BH data (and are therefore unconstrained).



Table 2: PG data used to fill holes in BH overlaps data.

ME+4/1/14 and ME+4/1/15
ME+3/2/18 and ME+3/2/19
ME+2/2/15 and ME+2/2/17 (16 has no BH or PG data)
ME+2/2/19 and ME+2/2/20
ME+2/1/01 and ME+2/1/02
ME+1/2/14, ME+1/2/15, and ME+1/2/16
ME+1/2/34, ME+1/2/36, and ME+1/2/01 (35 has no BH or PG data)
ME−1/2/04 and ME−1/2/05
ME−1/2/33 and ME−1/2/34
ME−2/1/06 and ME−2/1/07
ME−2/2/02, ME−2/2/03, and ME−2/2/04

## 4.5 Comparison of results with and without PG used to fill missing BH overlaps only

Since PG constraints are clearly needed to control floating groups of chambers such as those in ME+2/2, but might be unrealistically distorting the shapes of rings such as ME+3/2, it would be good to compromise by applying PG constraints only where they are needed: directly around the missing BH data. Referring to Fig. 3 to identify missing overlaps, we find that only 25 chambers strictly need to be constrained, out of 299 available constraints. These are listed in Table 2.

The results of an alignment using only these few constraints, compared to an alignment with all chambers constrained, are shown in Figs. 16 and 17. They look very similar to the comparison of non-PG-constrained with fully PG-constrained in Figs. 13 and 14, except that chambers 16–19 (inclusive) in ME+2/2 are not allowed to float freely with respect to the other chambers in this ring, and the discontinuity between chambers 18 and 19 in ME+3/2 is smaller— both of which are gaps in BH data.

The global distortions between minimally PG-constrained and fully PG-constrained alignments in ME±3/2 are presented graphically in Fig. 18. These are exaggerated pictorial representations (by a factor of 200) of the geometry differences, showing differences in  $x$ ,  $y$ , and  $\phi_z$ . The chambers are colored by  $x$  differences as a guide to the eye: the new information in this plot is the correlation between  $r\phi$  and  $\phi_z$  deviations, which are maximal at the bottom of the rings.

## 4.6 Ring radii measured from closure constraints

The first step in each beam-halo alignment is to adjust the radius of each ring such that the sum of  $r\phi$  residuals means is zero ( $\sum_i m_{ii+1} = 0$  for BH  $r\phi$  constraints). Without this correction, the alignment results would buckle to try to distribute the non-zero sum across non-uniform weights. Since we interpret this correction as a physical change in the radius of rings (expected in  $\vec{B} = 3.8$  T), these ring-radius corrections are also interesting results.

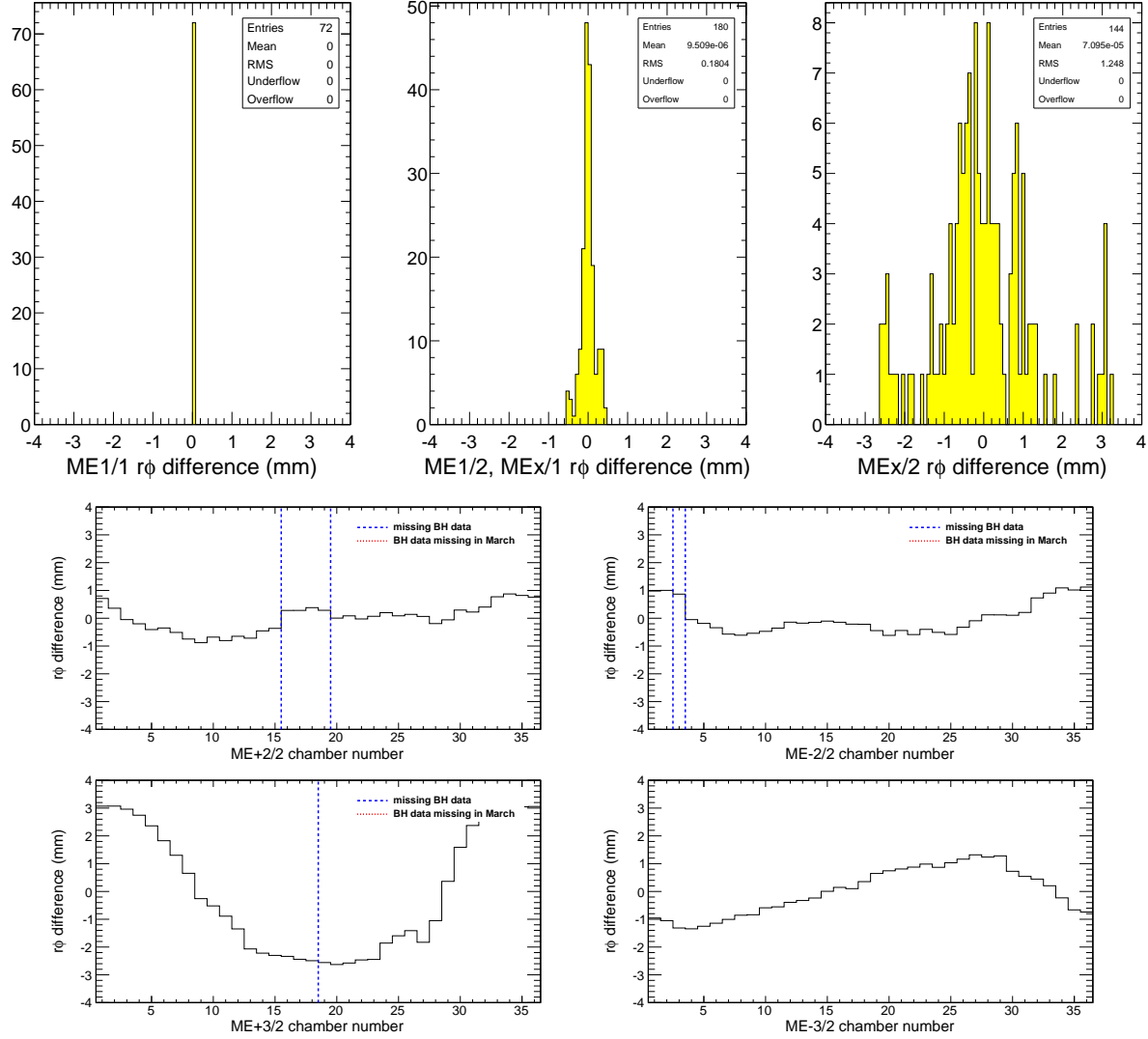


Figure 16: Differences in  $r\phi$  parameters between a summer 2010 alignment with and without PG measurements used to fill missing BH overlaps only. ME1/1 chambers have no PG constraint, so they are unaffected, and differences in inner-ring chambers are also negligible. However, the outer rings differ systematically. ME+2/2 has two missing BH overlaps that benefit from the PG constraint: with only these constraints applied, discontinuities at chambers 15-16 and 19-20 are less significant (compare with Fig. 13). Global distortions in ME $\pm$ 3/2 are unaffected.

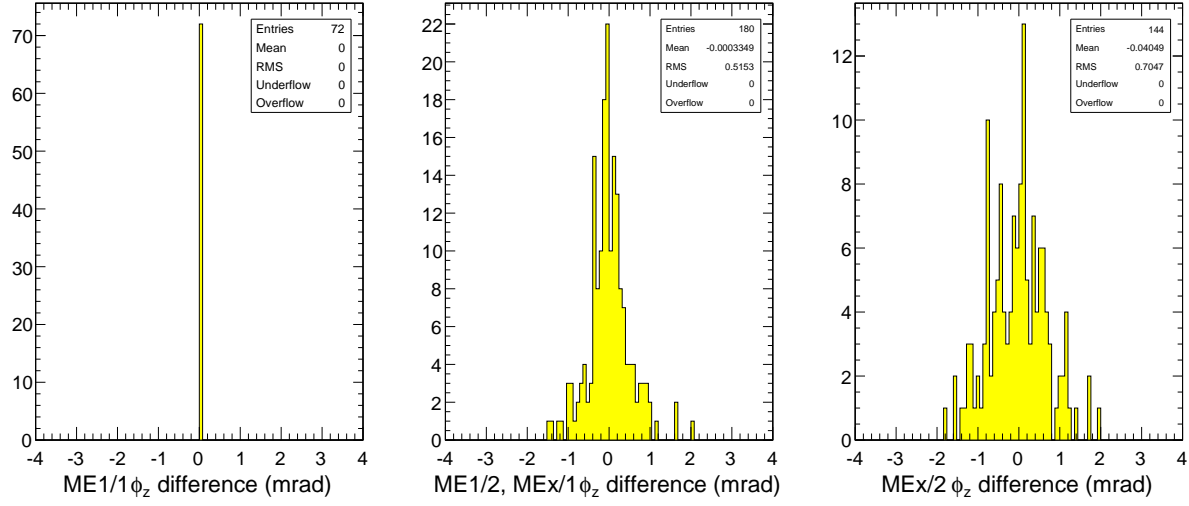


Figure 17: Differences in  $\phi_z$  parameters between a summer 2010 alignment with and without PG measurements used to fill the missing BH overlaps only. ME1/1 chambers have no PG constraint, so they are unaffected. Differences in other rings are at the level of 0.5–0.8 mrad (RMS).

Disk +3 (length x200, angle x200)

Disk -3 (length x200, angle x200)

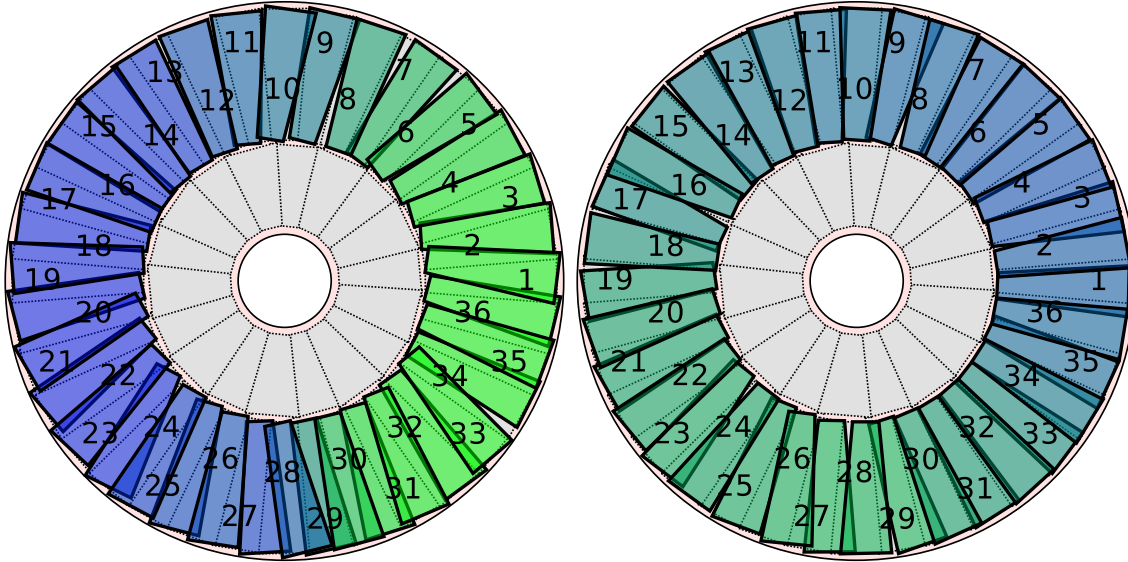


Figure 18: Differences in  $x$ ,  $y$ , and  $\phi_z$  between a summer 2010 alignment with and without PG measurements used to fill the missing BH overlaps only, for ME $\pm$ 3/2. The color gradation signifies the difference in  $x$ , and is meant to help the eye see the pattern of correlated  $x$  and  $\phi_z$  deviations near the bottom of ME+3/2. Compare to Fig. 16.

Table 3: Radius corrections relative to the following nominal values: ME1/1 1815 mm, ME1/2 3697 mm, ME2/1 2427 mm, ME2/2 5265 mm, ME3/1 2527 mm, ME3/2 5265 mm, ME4/1 2626.5 mm, where positive corrections mean that the radius must be made larger. The four geometries below are “PG only,” no beam-halo radius correction, “with old HW,” beam-halo alignment starting from the old hardware  $z/\phi_x$  pre-alignment, “with new HW,” beam-halo alignment starting from the new hardware  $z/\phi_x$ , “new HW and  $\phi_y$ ,” beam-halo alignment starting from the new hardware and non-zero  $\phi_y$  corrections from collisions.

	PG only	with old HW	with new HW	new HW and $\phi_y$
ME+1/1	0.0	−0.5	−0.5	−0.5
ME+1/2	0.3	1.8	0.8	0.7
ME+2/1	0.8	2.0	2.1	2.0
ME+2/2	1.0	−0.4	1.8	2.0
ME+3/1	−0.8	−1.3	−1.1	−1.1
ME+3/2	−0.3	−5.4	−2.0	−2.0
ME+4/1	−0.4	−1.2	−1.2	−1.2
ME−1/1	0.0	−1.7	−1.7	−1.7
ME−1/2	−0.3	0.4	0.4	0.3
ME−2/1	0.0	1.0	0.9	1.0
ME−2/2	0.7	−0.7	0.5	0.4
ME−3/1	−1.2	−2.0	−2.0	−2.0
ME−3/2	−0.7	−5.1	−3.8	−3.9
ME−4/1	−0.6	−1.5	−1.4	−1.5

Table 3 summarizes ring-radius corrections for all alignments considered in this note. It is worth noting that the new hardware description (believed to be more accurate than the old one for reasons not discussed here) significantly changes the apparent radius of some rings, in all cases making changes relative to design less extreme. Corrections to  $\phi_x$  can change the radial position of  $r\phi$  intercepts at the plane between pairs of chambers, modifying the apparent radius.

## 5 Conclusions and recommended geometry

The beam-halo overlaps alignment method is now a standard technique, having been applied four times since first LHC beams in 2008. Most recently, beam-halo data collected during summer 2010 collisions were analyzed. Seven ME1/1 chambers that were inoperative during the March 2010 dedicated beam-halo run are now available, and one chamber in ME−1/2 is now missing. Photogrammetry data are used to constrain rings with missing beam-halo data.

In this note, we studied differences in the apparent geometry between March and summer 2010, but due to changes in trigger conditions, collisions backgrounds, and available chambers, these differences cannot be conclusively identified as being real motions of the

detectors. In the case of ME+1/1, they can clearly be identified as improvements due to the addition of previously unavailable beam-halo data.

Since two new pre-alignments (hardware  $z/\phi_x$  and collisions  $\phi_y$ ) are to be applied to the new alignment, we studied the effect of applying each correction before beam-halo alignment. Differences were all significantly less than 1 mm in  $r\phi$  and 1 mrad in  $\phi_z$ . The new hardware correction has a significant influence on apparent ring-radii, though.

The photogrammetry constraint was studied in more detail than in previous alignment work, with three cases considered: (1) apply all PG data, (2) only apply PG data to fill in gaps in the BH data, and (3) apply no PG data. The alignment clearly suffers in case (3), most visibly in ME+2/2 (Fig. 13). Cases (1) and (2) only differ in the outer rings, as PG are not available in ME1/1 and inner rings are statistically dominated by BH data. Applying or not applying full PG data changes the global shapes of outer rings, especially ME+3/2. To determine whether the global distortion is a weak mode of the minimally PG-constrained alignment or a real coherent motion between 2007 and 2010, we should observe both in collisions data and look for the presence or absence of a 3 mm amplitude trend.

SQLite files representing the two cases can be found at:

- `/afs/cern.ch/user/p/pivarski/public/OCT23-PG-HW-phiy-BHPG.db` (1);
- `/afs/cern.ch/user/p/pivarski/public/OCT23-PG-HW-phiy-BHPGholes.db` (2).

One of these two will be proposed for the sign-off on Nov. 5, depending on the outcome of the test with collisions muons. It will also be necessary to apply disk corrections to finalize the alignment.